

Turbulent Aeroheating Testing of Mars Science Laboratory Entry Vehicle

Brian R. Hollis*

NASA Langley Research Center, Hampton, Virginia 23681

and

Arnold S. Collier†

Arnold Engineering Development Center, White Oak, Silver Spring, Maryland 20901

DOI: 10.2514/1.31798

An experimental investigation of turbulent aeroheating on the Mars Science Laboratory entry vehicle heat shield has been conducted in the Arnold Engineering Development Center Hypervelocity Wind Tunnel No. 9. Testing was performed on a 6 in. (0.1524 m) diameter Mars Science Laboratory model in perfect-gas N_2 in the tunnel's Mach 8 and Mach 10 nozzles at freestream Reynolds numbers of 4.1×10^6 – 49×10^6 ft (1.3×10^7 – 16×10^7 m) and 1.2×10^6 – 19×10^6 ft (0.39×10^7 – 62×10^7 m), respectively. These conditions were sufficient to span the regime of boundary-layer flow from completely laminar to fully developed turbulent flow over the entire forebody. A supporting aeroheating test was also conducted in the Langley Research Center 20 Inch Mach 6 Air Tunnel at freestream Reynolds numbers of 1×10^6 – 7×10^6 ft (0.36×10^7 – 2.2×10^7 m) to help corroborate the Tunnel 9 results. A complementary computational fluid dynamics study was conducted in parallel to the wind-tunnel testing. Laminar and turbulent predictions were generated for the wind-tunnel test conditions and comparisons were performed with the data for the purpose of helping to define uncertainty margins on predictions for aeroheating environments during entry into the Martian atmosphere. Data from both wind-tunnel tests and comparisons with the predictions are presented herein. It was concluded from these comparisons that for perfect-gas conditions, the computational tools could predict fully laminar or fully turbulent heating conditions to within $\pm 12\%$ or better of the experimental data.

Nomenclature

a	=	speed of sound, m/s
c_p	=	specific heat of test gas, J/kg · K
c_{pm}	=	specific heat of model material, J/kg · K
D	=	maximum vehicle diameter, m
k_m	=	thermal conductivity of model material, W/m · K
L/D	=	aerodynamic lift-to-drag ratio
M_∞	=	freestream Mach number
M_e	=	boundary-layer edge Mach number
n	=	height of wall cell in computation grid, m
p_∞	=	freestream pressure, Pa
q	=	heat transfer rate, W/m ²
R_{base}	=	base (maximum) radius, m
R_{corner}	=	corner radius, m
R_{nose}	=	nose radius, m
Re_∞	=	freestream unit Reynolds number, 1/m
$Re_{\infty,D}$	=	freestream Reynolds number based on diameter
Re_θ	=	boundary-layer momentum thickness Reynolds number, $\rho_e U_e \theta / \mu_e$
St	=	Stanton number
T_∞	=	freestream temperature, K
U_e	=	boundary-layer edge velocity, m/s
U_∞	=	freestream velocity, m/s
x/R	=	normalized distance along model centerline
α	=	angle of attack, deg

ΔH	=	total enthalpy relative to wall conditions, J/kg
θ	=	boundary-layer momentum thickness, m
θ_{aft1}	=	first aftbody cone half-angle, deg
θ_{aft2}	=	second aftbody cone half-angle, deg
θ_F	=	forebody cone half-angle, deg
μ_e	=	boundary-layer edge viscosity, kg/m · s
μ_∞	=	freestream viscosity, kg/m · s
ρ_e	=	boundary-layer edge density, kg/m ³
ρ_m	=	density of model material, kg/m ³
ρ_∞	=	freestream density, kg/m ³

Subscripts

∞	=	freestream
e	=	boundary-layer edge
m	=	material
w	=	wall

I. Introduction

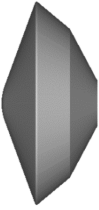
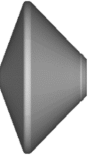

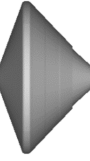
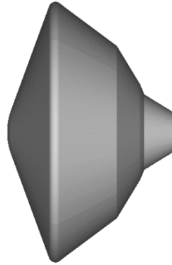
THE Mars Science Laboratory (MSL) mission [1,2], which is scheduled to be launched in 2009, will perform a precision landing of a large (>3000 kg) scientific payload on the surface of Mars in 2010. Although the basic vehicle configuration, a 70 deg sphere-cone forebody with a conic or biconic aftbody, will be similar to those of previous Mars missions such as Viking, Pathfinder, or Mars Exploration Rover (MER), the MSL design is both larger and heavier than previous designs (Table 1). To accomplish a precision landing, the vehicle will be required to fly a controlled lifting trajectory; current designs call for a lift-to-drag ratio (L/D) of 0.24, which will be generated by flying at an angle of attack of -16 deg. As a result of its high ballistic coefficient, MSL will experience heating levels higher than any of the previous missions and, furthermore, because of the high angle-of-attack (for a blunt body) flight requirement, the flow over the lee side of the forebody is expected to become turbulent early in the trajectory, which will substantially augment both the heating rates and loads above laminar levels [3].

Presented as Paper 1208 at the 45th AIAA Aerospace Sciences Meeting and Exhibit, Reno, NV, 8–11 January 2007; received 16 May 2007; revision received 29 October 2007; accepted for publication 12 November 2007. This material is declared a work of the U.S. Government and is not subject to copyright protection in the United States. Copies of this paper may be made for personal or internal use, on condition that the copier pay the \$10.00 per-copy fee to the Copyright Clearance Center, Inc., 222 Rosewood Drive, Danvers, MA 01923; include the code 0022-4650/08 \$10.00 in correspondence with the CCC.

*Aerospace Engineer, Aerothermodynamics Branch, AIAA Senior Member.

†Project Engineer.

Table 1 Comparison of Mars entry vehicles

	Viking 1 & 2	Pathfinder	MER A & B	Phoenix	MSL (as of 2007)
Configuration					
Diameter, m	3.5	2.65	2.65	2.65	4.5
Entry mass, kg	930	585	840	602	>3000
Landed mass, kg	603	360	539	364	>1700
Relative entry vel., km/s	4.5/4.42	7.6	5.5	5.9	>5.5
Relative entry angle, deg	−17.6	−13.8	−11.5	−13	−15.2
Ballistic coefficient, kg/m ²	63.7	62.3	89.8	65	>140
Turbulent at peak heating?	No	No	No	No	Yes
Peak heat flux, W/cm ²	24	115	54	56	>200
Hypersonic α , deg	−11.2	0	0	0	−15.5
Hypersonic L/D	0.18	0	0	0	0.24

Because there are relatively little data on the turbulent heating of very large-angle blunt cones such as the MSL entry vehicle, an extensive test program has been conducted to produce data with which the accuracy of computational fluid dynamics (CFD) tools used to predict flight environments can be compared. To date, tests have been performed [4–7] in the NASA Langley Research Center (LaRC) 20 Inch Mach 6 Air Tunnel (heat-shield penetration effects, perfect-gas environments, transition onset), the Calspan University of Buffalo (CUBRC) Large-Energy National Shock (LENS) Tunnel (low-to-moderate enthalpy reacting CO₂ environments, transition onset, and turbulent heating), and the Graduate Aeronautical Laboratories of the California Institute of Technology (GALCIT) T5 Hypervelocity Shock Tunnel (moderate to high-enthalpy reacting CO₂ environments and turbulent heating).

The test detailed herein was performed in perfect-gas N₂ in the Arnold Engineering Development Center (AEDC) Tunnel 9. Data were obtained across a very wide range of Reynolds numbers to evaluate the accuracy of CFD tools at predicting turbulent flows in an environment free from the chemical nonequilibrium effects present in the CUBRC LENS and GALCIT T5 tests. In addition to the AEDC Tunnel 9 test, a small amount of data were also obtained in the LaRC 20 Inch Mach 6 Air Tunnel using the same wind-tunnel model for comparison to the AEDC results. These two tests are expected to complete the heat-shield aeroheating test program.

II. Experimental Method

A. Facility Descriptions

1. AEDC Tunnel 9 Description

The U.S. Air Force's Arnold Engineering Development Center Tunnel 9, located in Silver Spring, Maryland, is a hypersonic, nitrogen-gas, blowdown wind tunnel with interchangeable nozzles that allow for testing at Mach numbers of 7, 8, 10, and 14 over a 0.054×10^6 – 48.4×10^6 ft (0.177×10^6 – 158.8×10^6 m) unit Reynolds number range. A schematic drawing of the facility is shown in Fig. 1 and a full description of the facility can be found in [8]. The test section is a 5 ft (1.52 m) diameter, 12 ft (3.66 m) long cell that enables testing of large-scale model configurations. Tunnel 9 features a pitch system that can sweep models from −10 to 50 deg at pitch rates up to 80 deg/s. With the tunnel's 0–15 s run times, the dynamic pitch capability allows for a large volume of data to be captured over an entire range of pitch angles during a single run.

2. NASA LaRC 20 Inch Mach 6 Air Tunnel Description

The NASA Langley Research Center 20 Inch Mach 6 Air Tunnel is a blowdown facility in which heated, dried, and filtered air is used

as the test gas. The tunnel has a two dimensional, contoured nozzle that opens into a 0.521×0.508 m (20.5 × 20.0 in.) test section. The tunnel is equipped with a bottom-mounted injection system that can transfer a model from the sheltered model box to the tunnel centerline in less than 0.5 s. Run times of up to 15 min are possible in this facility, although for the current aeroheating study, run times of only a few seconds were required. The nominal reservoir conditions of this facility are stagnation pressures of 206.8–3447.4 kPa (30–500 psia) with stagnation temperatures of 422.2–555.5 K (760–1000°R), which produce perfect-gas freestream flows with Mach numbers between 5.8 and 6.1, and Reynolds numbers of 1.64×10^6 – 23.3×10^6 m (0.5×10^6 – 7.3×10^6 ft). A more detailed description of this facility is presented in [9].

B. Test Parametrics

1. AEDC Tunnel 9 Test Parametrics

The primary focus of this study was a 22 run test performed in Tunnel 9, with seven runs in the tunnel's Mach 10 nozzle and 15 runs in the Mach 8 nozzle. The run matrix for this test is presented in Table 2. The Mach 10 runs (3020–2026) spanned a freestream Reynolds number range of 1.2×10^6 – 19.1×10^6 ft and the Mach 8 runs spanned a range of 4.1×10^6 – 49.6×10^6 ft. All Mach 10 runs were performed in continuous pitch-sweep data acquisition mode over a nominal range of 0–26 deg, although the span was reduced somewhat at the higher Reynolds numbers due to shorter run times. The initial Mach 8 runs (3027–3030) were also performed with a continuous pitch sweep over the same range, but it was found that the duration of good flow was shorter than expected and data at the beginning and end of the runs showed signs of transient behavior.

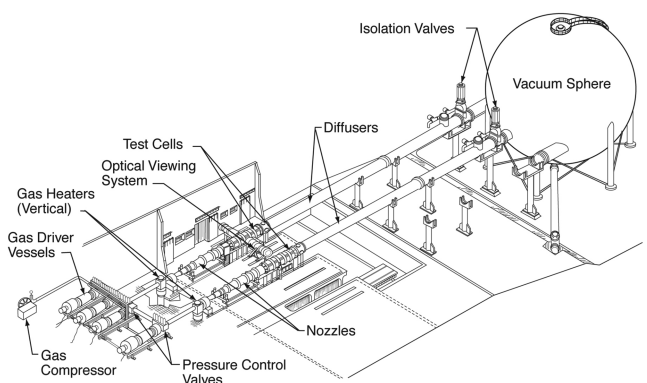
**Fig. 1 AEDC Tunnel 9 schematic.**

Table 2 AEDC Tunnel 9 run matrix (nominal run-averaged conditions)

Run	Re_∞ , 1/ft	M_∞	P_∞ , Pa	T_∞ , K	ρ_∞ , kg/m ³	U_∞ , m/s	ΔH , MJ/kg	α , deg
Mach 10 nozzle conditions (sorted by increasing Reynolds number)								
3021	1.18E + 06	9.47	167.9	54.8	0.0103	1428.0	0.765	0–26
3020	1.85E + 06	9.56	285.1	58.1	0.0165	1486.3	0.853	0–26
3022	4.62E + 06	9.80	656.1	54.4	0.0406	1474.9	0.832	0–26
3023	8.61E + 06	10.03	1068.3	51.9	0.0694	1472.5	0.826	0–26
3024	1.46E + 07	10.22	1696.2	50.2	0.1139	1475.5	0.829	0–20
3026	1.85E + 07	10.31	2079.3	49.5	0.1416	1479.2	0.833	5–24
3025	1.91E + 07	10.32	2068.1	48.3	0.1444	1461.8	0.807	0–18
Mach 8 nozzle conditions (sorted by increasing Reynolds number)								
3028	4.13E + 06	7.41	1162.5	73.5	0.0533	1294.2	0.602	0–26
3027	8.03E + 06	7.43	2302.3	74.6	0.1040	1308.8	0.622	0–26
3042	8.52E + 06	7.45	2366.9	73.1	0.1091	1298.6	0.607	0
3029	1.59E + 07	7.64	4988.8	80.7	0.2082	1398.3	0.750	0–26
3049	1.61E + 07	7.64	4968.0	79.8	0.2097	1391.7	0.739	8–19
3050	1.65E + 07	7.65	5078.3	79.8	0.2145	1391.8	0.740	12–22
3043	1.65E + 07	7.65	4470.0	73.2	0.2059	1334.0	0.654	0
3044	2.15E + 07	7.80	5407.0	70.4	0.2589	1333.0	0.650	0
3030	2.16E + 07	7.77	6158.7	76.6	0.2709	1386.0	0.728	0–25
3051	2.18E + 07	7.77	6235.2	76.6	0.2742	1386.8	0.729	8–19
3052	2.23E + 07	7.79	5966.0	73.4	0.2739	1359.1	0.688	12–22
3047	3.04E + 07	7.75	8231.8	73.8	0.3760	1356.4	0.685	16
3053	3.06E + 07	7.75	7989.6	71.9	0.3742	1339.3	0.660	9–20
3045	4.50E + 07	7.93	11824.6	73.4	0.5426	1383.0	0.721	0
3048	4.96E + 07	7.98	11918.6	69.3	0.5792	1350.9	0.673	16

Table 3 LaRC 20 Inch Mach 6 Air Tunnel run matrix

Run	Re_∞ , 1/ft	M_∞	P_∞ , Pa	T_∞ , K	ρ_∞ , kg/m ³	U_∞ , m/s	ΔH , MJ/kg	α , deg
5	1.08E + 06	5.89	297	61.3	0.0169	924.3	0.179	16
6	1.39E + 06	5.92	381	61.6	0.0216	931.4	0.186	16
4	2.13E + 06	5.96	584	61.8	0.0329	939.4	0.194	16
3	4.02E + 06	6.01	1100	61.9	0.0620	945.7	0.200	16
2	5.85E + 06	6.03	1633	62.9	0.0906	956.4	0.211	16
1	6.92E + 06	6.04	1939	63.2	0.1073	959.1	0.214	16

Several Mach 8 runs (3042–3049) were then performed at fixed angle of attack (0 or 16 deg) to define the period of acceptable flow quality at each condition. Additional runs (3050–3053) with shorter pitch sweeps centered in the high-quality flow period were then performed to span the range of ~8 to 22 deg angle of attack required by the MSL program.

In general, the Mach 10 conditions produced laminar flow except at the 15×10^6 ft condition (run 3024) where lee-side transition was clearly evident and at the 19×10^6 ft condition (runs 3025 and 3026) where turbulent lee-side flow was produced. At Mach 8, laminar flow was produced at the lowest 4×10^6 ft condition (run 3028), transitional flow at the 8×10^6 ft condition (runs 3027 and 3042), and turbulent flow at the higher Reynolds numbers.

2. NASA LaRC 20 Inch Mach 6 Air Tunnel Test Parametrics

A short test was also performed in the LaRC 20 Inch Mach 6 Air Tunnel to support the AEDC study. The purpose of this test was to confirm assumptions (to be detailed subsequently) made about thermal properties employed in the thermocouple data reduction process. Runs were performed at Mach 6 over a Reynolds number range of 1.1×10^6 – 6.9×10^6 ft. The matrix for this test is presented in Table 3.

C. Wind-Tunnel Model Design

A 6-in.-diam (0.1524 m) model of the MSL Outer Mold Line-6 (OML) configuration was fabricated from heat-treated 15–5 stainless steel (Figs. 2 and 3). As the flight vehicle configuration has been continuously evolving since the design of the test model, the OML-6 test configuration is different from the current OML-12 flight configuration. However, the differences are in the aftbody geometry

and, because the primary purpose of this study was to measure forebody heating rates, these differences are not relevant to this study.

The test model was instrumented with 39 Type-E coaxial (chromel-constantan) thermocouples. This type of sensor is routinely



Fig. 2 Close-up view of MSL model in NASA LaRC 20 Inch Mach 6 Air Tunnel (retracted into model box).

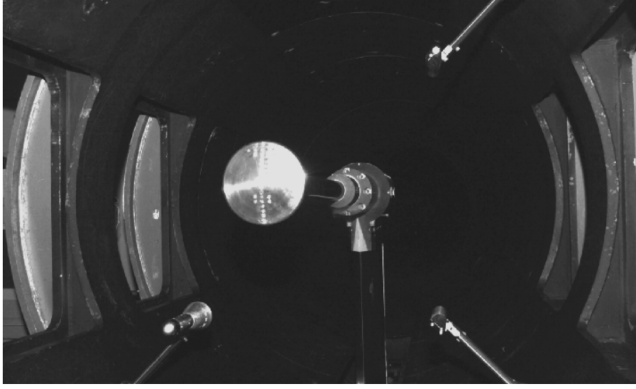


Fig. 3 MSL model installed in AEDC Tunnel 9.

used in the AEDC Tunnel 9 facility for aerothermal studies [10]. A schematic gauge layout is shown in Fig. 4. Of the gauges, 33 of the 39 were located on the forebody and the remaining gauges were located on the aftbody along the centerline. Of the forebody gauges, 19 were evenly distributed along the centerline, with additional gauges off-centerline in the wind-side stagnation region and outboard on the lee side where the widest growth of the turbulent heating region occurs.

The thermocouples were fitted into the model through predrilled holes and fixed with adhesive, then sanded carefully to form the required chromel-constantan electrical junctions and to match the surface contours of the model. The shell thickness of the model (and the thermocouple length) was specified at a nominal value of 0.5 in. (slightly less at the corners) to ensure that heat-conduction into the model did not violate the semi-infinite assumption (conduction does not reach the interior face) over the length of the AEDC Tunnel 9 test time, which is on the order of 1 s or less.

D. Data Acquisition and Reduction

Thermocouple voltage data from AEDC Tunnel 9 were acquired at a frequency of 500 Hz and analog-filtered at 30 Hz to eliminate 60 Hz analog noise (data from the LaRC 20 Inch Mach 6 Air Tunnel were

acquired at 40 Hz). Voltage data were converted to temperatures via the National Institute of Standards and Technology (NIST) standard calibration formula for Type-E thermocouples. These data were then used to compute heat transfer rates through a one-dimensional finite difference numerical method. Descriptions of these methods can be found in [10–12]. As a check on the data reduction process, the test data were reduced using both LaRC and AEDC software tools QCALC [11] and 1DHEAT [12], and the results from both codes were in very close agreement.

These conduction analysis methods produce a time history of the dimensional heat transfer rate, which is a function of both the freestream conditions and the model surface temperature. Because the freestream conditions in Tunnel 9 vary slightly over the course of the run, and because the rise in model surface temperature can be nonnegligible with respect to the stagnation temperature (which drives the convective heating), especially for the high Reynolds number Mach 8 conditions, the heat transfer rate is not necessarily the ideal parameter with which to report the test data. Therefore, results are presented herein in terms of the product of the Stanton number times the square root of the Reynolds number, $St \times (Re_{\infty,D})^{0.5}$, which is defined as

$$St \times (Re_{\infty,D})^{1/2} = \frac{q}{\rho_{\infty} U_{\infty} \Delta H} \sqrt{\frac{\rho_{\infty} U_{\infty} D}{\mu_{\infty}}} \quad (1)$$

where

$$\Delta H = c_p T_{\infty} + \frac{U_{\infty}^2}{2} - c_p T_w \quad (2)$$

This nondimensional quantity is very nearly a constant over the course of the run (assuming that the angle of attack is held fixed); the ΔH and q terms balance each other as the wall temperature increases, whereas the ρ_{∞} and U_{∞} terms account for variations in flow conditions over the run. Also, multiplication by the square root of the Reynolds number results in a term that has only a very slight dependence on Reynolds number for laminar flows (for turbulent flows, an exponent of 0.2 on the Reynolds number is frequently employed). When heating distributions are expressed in terms of this

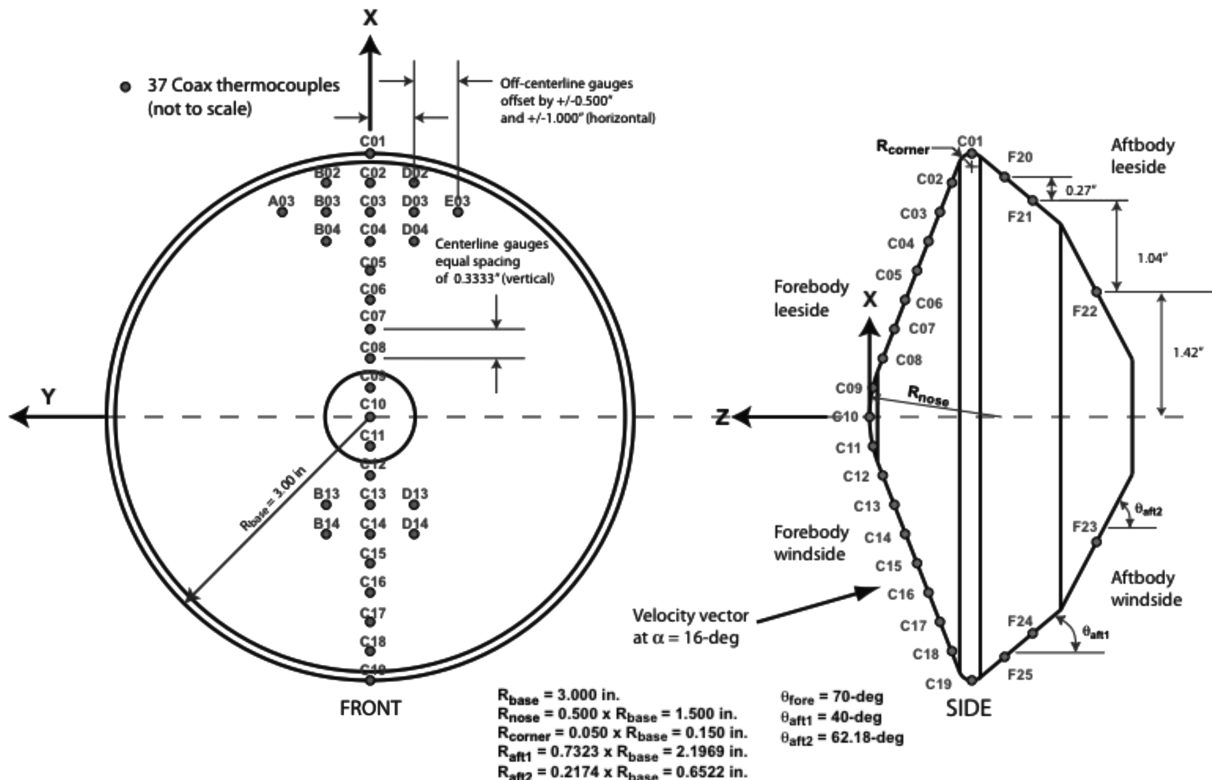


Fig. 4 MSL model dimensions and thermocouple layout.

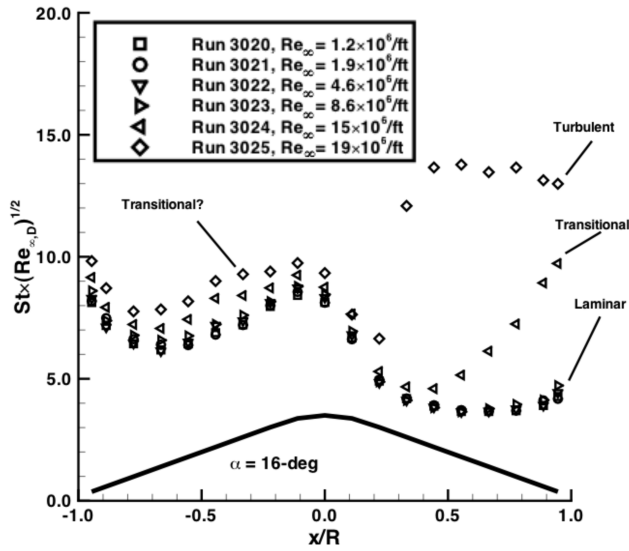


Fig. 5 Correlation of centerline heating distribution vs freestream Reynolds number.

parameter, it can be used to correlate laminar heat-flux distributions over the range of test conditions. Transitional/turbulent data can then clearly be identified when the values diverge from the lower Reynolds number laminar data, such as shown in Fig. 5. It should be noted that this parameter is sometimes defined in other studies using edge conditions instead of freestream conditions for the density and velocity, and the adiabatic or reference wall enthalpy instead of the total enthalpy.

E. Wind-Tunnel Model Material Properties

The data reduction methods discussed in the previous sections require specification of the thermal properties of the wind-tunnel model to determine heat transfer rates from the temperature-time history. Thermal property data can be obtained from several sources (as cited in [10–12]). However, the accuracy of these data is hard to assess and the use of different data sets has a significant effect on the resulting heating levels, as shown in the example in Fig. 6. The conduction analysis was initially performed using material thermal property data for chromel because the primary material of a Type-E chromel-constantan thermocouple is chromel. However, the resulting experimental heating levels were found to be well in excess of predicted levels: more than 20% higher than predictions, which is not reasonable for laminar, perfect-gas flow over a relatively simple shape. These differences suggested a problem with the thermal property data used in the analysis. This problem was verified by two independent experimental investigations:

1) Thermocouples were installed into stainless steel and chromel plugs on a flat plate adjacent to NIST-traceable heat-flux calorimeters and then bench-tested under a calibrated radiant lamp [13].

2) The MSL wind-tunnel model was tested in the NASA LaRC 20 Inch Mach 6 Air Tunnel to rule out any facility-related issues such as flow quality, model installation, and instrumentation hookup, signal acquisition, filtering, and recording, etc.

As a result of these tests, it was found that the use of material thermal property curve fits used by AEDC for 17–4 stainless steel (instead of chromel or 15–5 stainless steel) provided the best match with the calibrated heat source. When data from both AEDC Tunnel 9 and the NASA LaRC 20 Inch Mach 6 Air Tunnel were reduced using these properties, a close match with predictions was obtained. Curve fits for these properties are given in Eqs. (3–5). Furthermore, because the calibration study [13] revealed a consistent bias of approximately +3% in the coaxial thermocouple data in comparison with the calibration standard, the final data generated for this study were postprocessed to remove that bias. The reason for the better fit obtained using 17–4 thermal properties has not yet been conclusively determined; it may be possible that the heat transfer process within the model is dominated by the much larger thermal

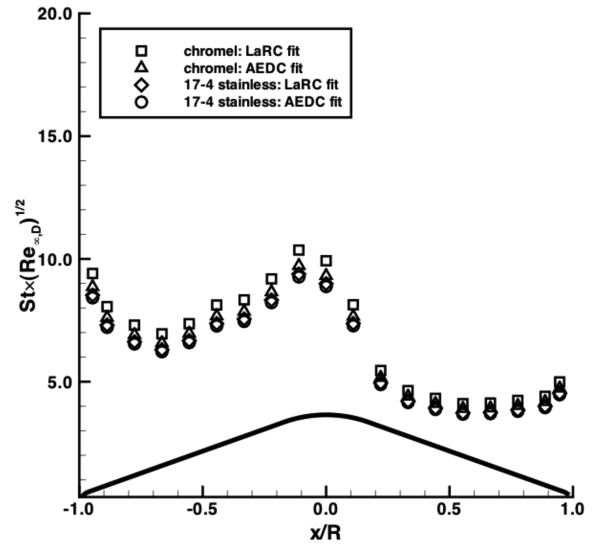


Fig. 6 Variation in heating due to choice of thermal properties used in data reduction.

mass of the model itself, or it may be that the available data on the thermal properties of the thermocouple is simply wrong and the actual values are coincidentally closer to those for available for 17–4 stainless steel. In any case, the 17–4 thermal properties given here provide the best fit with both calibration data and predictions, and their use is recommended in the interim until a more detailed investigation into material thermal properties can be conducted.

AEDC 17–4 stainless steel thermal property curve fits are as follows:

$$\rho_m = 7805.7 \text{ kg/m}^3 \quad (3)$$

$$c_{pm} = 409.76 - 5.3809 \times 10^{-2} T + 6.0366 \times 10^{-4} \text{ J/kg} \cdot \text{K} \quad (4)$$

$$k_m = 11.665 + 1.52078 \times 10^{-2} T \text{ W/m} \cdot \text{K} \quad (5)$$

F. Experimental Uncertainty

The experimental uncertainty of the heat transfer data is clearly very dependent on the selection of material properties. As shown in the previous section, this uncertainty is on the order of ± 10 –20%. This error source could be lowered, at least in theory, through a more detailed statistically based study of material properties, but such a study is outside the scope of the MSL project. Separate from this source are uncertainties due to variations in freestream conditions, model angle of attack, and instrumentation precision. For heat transfer testing with Type-E thermocouples on a blunt configuration such as MSL, an uncertainty of $\pm 6\%$ (not including thermal properties) for these factors is quoted as a standard by AEDC. Although no formal analysis was performed for the LaRC Mach 6 tunnel because the use of thermocouples there is so rare, the flow conditions are more steady than those in Tunnel 9 due to the method of operation, and so the uncertainty should be no more than that estimated for Tunnel 9. Taking into account the independent assessment of material thermal properties with a calibrated heat source, and the generally good agreement with predictions obtained in both wind tunnels, it is recommended that an estimate for material properties uncertainty of $\pm 10\%$ be combined with the quoted AEDC uncertainty of $\pm 6\%$ to give a root-mean-squared uncertainty of $\pm 11.66\%$, which can be rounded up to $\pm 12\%$ for simplicity.

III. Computational Method

Flowfield computations at the wind-tunnel test conditions were performed using the LAURA (Langley Aerothermodynamic Upwind Relaxation Algorithm) code [14,15]. The LAURA code is

a three-dimensional, finite volume solver that includes perfect-gas, equilibrium, and nonequilibrium chemistry models. The code can be used to solve the inviscid, viscous thin-layer Navier–Stokes, or full Navier–Stokes equations. For the current study, the thin-layer model was employed. It was concluded in [4] from computations on a similar blunt body that this model provided accurate results for attached forebody flows. Time integration to steady state in LAURA is accomplished through a combination of line- and point-relaxation schemes. Roe averaging [16] with Harten’s entropy fix [17] and Yee’s symmetric total variation diminishing limiter [18] is used for inviscid fluxes, and a second-order scheme is employed for viscous fluxes. In this study, a perfect-gas model was used for the AEDC and LaRC tunnel conditions with the appropriate gas parameters for either pure N_2 (AEDC Tunnel 9) or air (LaRC 20 Inch Mach 6 Air).

For the AEDC CFD cases, freestream conditions were extracted from the data set for that run at the time at which the specified angle of attack was reached because the freestream conditions do vary over the length of a run. For the wall boundary condition, a uniform temperature over the body equal to that recorded at the nose gauge (C10) at the specified time during the run was used. For the LaRC 20 Inch Mach 6 Air wind-tunnel cases, freestream conditions do not vary significantly over the length of the run, and so the nominal conditions in Table 3 could be used. The wall temperature boundary condition was specified in the same manner as for the AEDC CFD cases.

Structured, finite volume, multiple-block forebody grids with a singularity-free nose were employed for the computations. The grid topology matches that used in flight computations [3], as well as in previous wind-tunnel studies [4]. Grid adaptation was performed (as per the method detailed in [15]) to align the grid with the bow shock and to produce nominal wall cell Reynolds numbers on the order of one. Grid resolution requirements for MSL computations have been determined through many past studies (e.g., [4]).

Laminar computations were performed for AEDC and LaRC tunnel cases. Turbulent computations were performed for several cases using the algebraic Cebeci–Smith turbulence model (the algebraic Baldwin–Lomax model was used for a few selected AEDC cases and found to produce only slightly different results for these perfect-gas conditions). Although it is recognized that more sophisticated turbulent models exist, different models can produce very different results (e.g., [19]) and the validation status of any and all turbulence models for hypersonic flow over a given vehicle type is debatable. Algebraic models are the standard being used for MSL flight database development because they are computationally fast and stable, and, as will be shown subsequently, the accuracy of algebraic model turbulent predictions on the forebody, at least for the conditions under consideration, is generally as good as that of the laminar predictions.

IV. Results and Analysis

A. AEDC Tunnel 9 Data

The AEDC test was conducted in a continuous-pitch mode and so heating data were obtained over the entire angle-of-attack range of each run ($\sim 26^\circ$ at Mach 10 or $\sim 10^\circ$ at Mach 8). Values at a specific angle of attack were extracted from the data set by averaging over a time interval encompassing $\pm 0.5^\circ$ in pitch from the specified value. This data set is far larger than can be presented herein, and so, for the purposes of this report, this discussion will focus on the forebody $\alpha = 16^\circ$ data because that is the current trim angle for flight.

A sampling of the data obtained over the complete pitch-sweep range is given in Figs. 7 and 8 for the Mach 10 conditions and in Figs. 9 and 10 for the Mach 8 conditions, in which data are presented for both low and high Reynolds number runs in each nozzle. The Mach 10 data shown indicate laminar behavior for all α at the $Re_\infty = 1 \times 10^6$ ft condition (Fig. 7) and transitional or fully turbulent behavior on the lee side ($x/R > 0$) at the $Re_\infty = 19 \times 10^6$ ft condition (Fig. 8) depending on α . For the Mach 8 Reynolds number cases shown, the data appear to be transitional or fully turbulent on the lee side for all α at both Reynolds numbers, except possibly at the lowest α values at the $Re_\infty = 8 \times 10^6$ ft condition

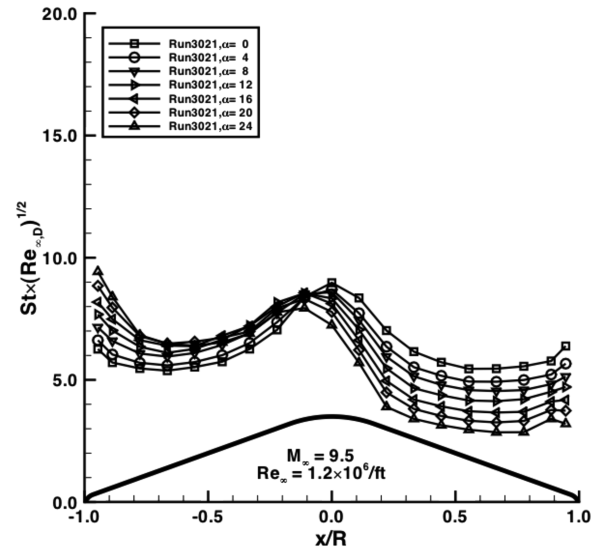


Fig. 7 Angle-of-attack effects, Mach 10 nozzle, $Re_\infty = 1 \times 10^6$ 1/ft.

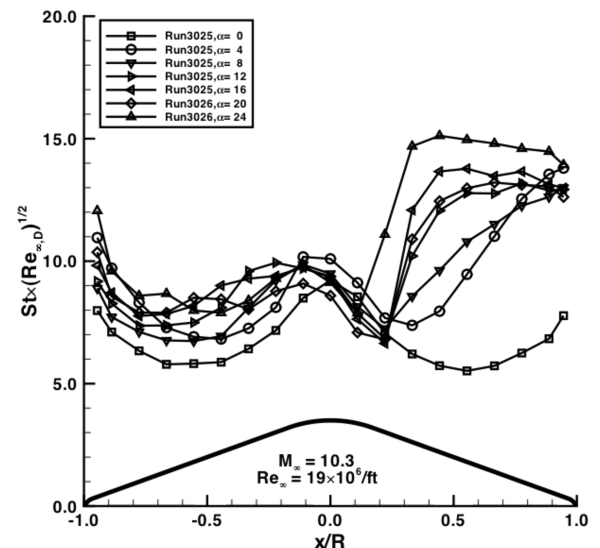


Fig. 8 Angle-of-attack effects, Mach 10 nozzle, $Re_\infty = 19 \times 10^6$ 1/ft.

(Fig. 9). Both the wind-side and lee-side data at the Mach 8, $Re_\infty = 22 \times 10^6$ ft condition (Fig. 10) appear to be transitional or turbulent.

Although the purpose of this study was not to formulate or validate transition criteria, some insight into the transitional/turbulent behavior of the data can be gained by examining boundary-layer parameters such as Re_θ and Re_θ/M_e . Computed values of these parameters for $\alpha = 16^\circ$ at the Mach 10 and Mach 8 nozzle conditions are plotted in Figs. 11 and 12. Note that in the computations of these parameters, the boundary-layer edge is defined as the point where the total enthalpy is 99.95% of that in the freestream. Previous studies [7] have indicated that transition occurs between values of 200–400 for Re_θ/M_e , whereas the design specification [3] for the MSL program is to assume turbulent flow in flight for values of Re_θ greater than 200, which occurs well before the peak heating point on current design trajectories. Conditions in both nozzles exceed these values (by a great deal in the Mach 8 nozzle), which provides evidence that the data at higher Reynolds numbers can be interpreted as fully turbulent.

Comparisons between the tunnel data and CFD predictions along the centerline of the model are presented in Figs. 13–18 for the Mach 10 conditions and in Figs. 19–24 for the Mach 8 conditions. Error bars on the wind-tunnel data in these figures correspond to the $\pm 12\%$ estimate previously discussed. When available, data from repeat runs are also plotted, although the error bars are shown for only one of the data sets to make the plots readable.

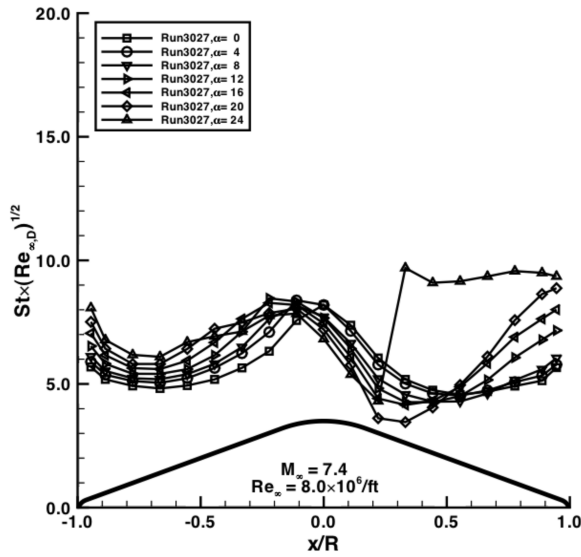


Fig. 9 Angle-of-attack effects, Mach 8 nozzle, $Re_{\infty} = 8 \times 10^6$ 1/ft.

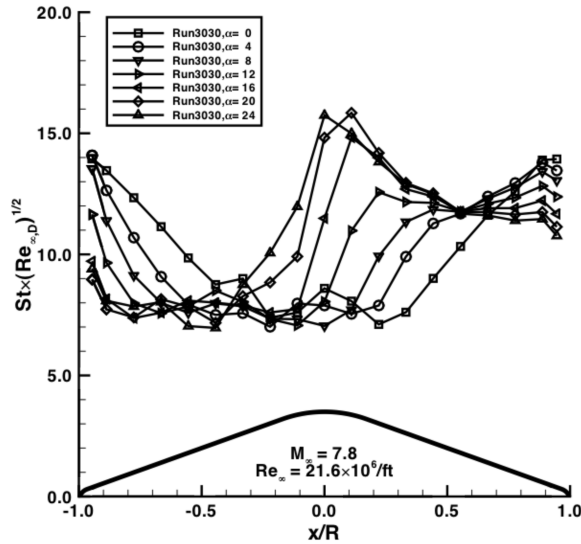


Fig. 10 Angle-of-attack effects, Mach 8 nozzle, $Re_{\infty} = 22 \times 10^6$ 1/ft.

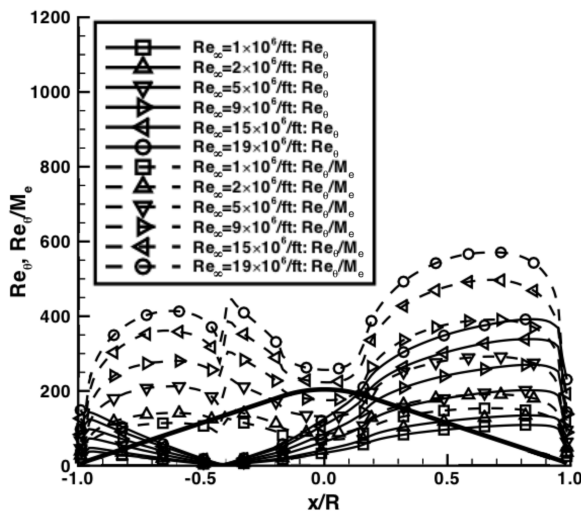


Fig. 11 Boundary-layer parameters for AEDC Tunnel 9 Mach 10 nozzle conditions.

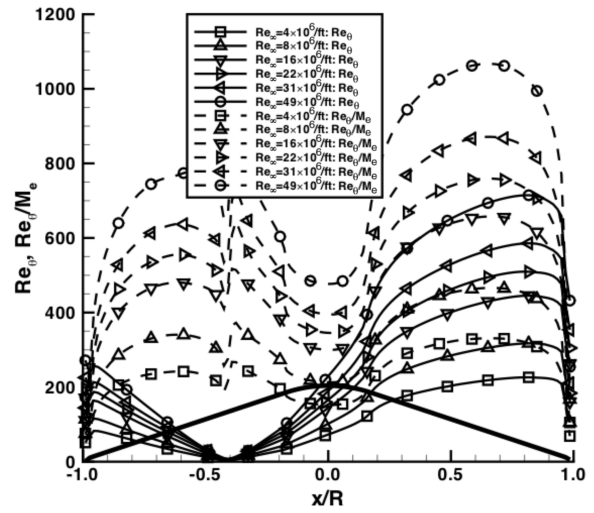


Fig. 12 Boundary-layer parameters for AEDC Tunnel 9 Mach 8 nozzle conditions.

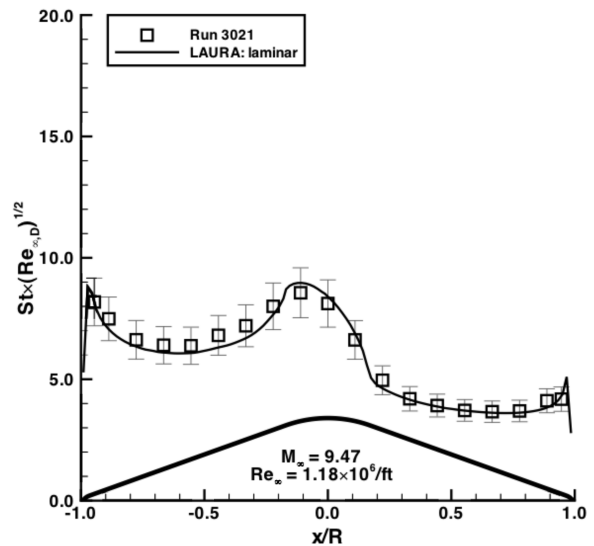


Fig. 13 Comparison for Mach 10 nozzle, $Re_{\infty} = 1.12 \times 10^6$ 1/ft, $\alpha = 16$ deg.

Both laminar and, where appropriate, turbulent predictions are shown in these figures. The turbulent predictions were made assuming fully developed turbulent flow over the entire forebody, whereas, in the actual test, fully developed turbulent flow was only produced over portions of the lee side of the vehicle at Mach 10 and over portions of the wind side and most of the lee side at Mach 8. Although it would have been possible to set a transition onset location in the algebraic turbulence models used for the predictions to better match the observed range of boundary-layer behavior, this option was not employed in the current analysis because the transition locations were not known a priori. In theory, it would be possible to develop a transition onset criterion from the current data set, and then use that result to specify transition onset for the computational methods, but such a step was beyond the scope of the current study.

The data from the four lowest Mach 10 Reynolds number cases (Figs. 13–16) appeared to all be laminar, and, for these cases, the predictions and data matched to within less than the $\pm 12\%$ experimental uncertainty for almost all data points. The lee-side transitional data for the next-to-highest case (Fig. 17, $Re_{\infty} = 14.6 \times 10^6$ ft) were higher than the laminar prediction, and for the lee side at the highest case (Fig. 18, $Re_{\infty} = 18.5 \times 10^6$ ft), the turbulent prediction matched the lee-side centerline data. For these two cases, there were also slight indications of a nonlaminar heating

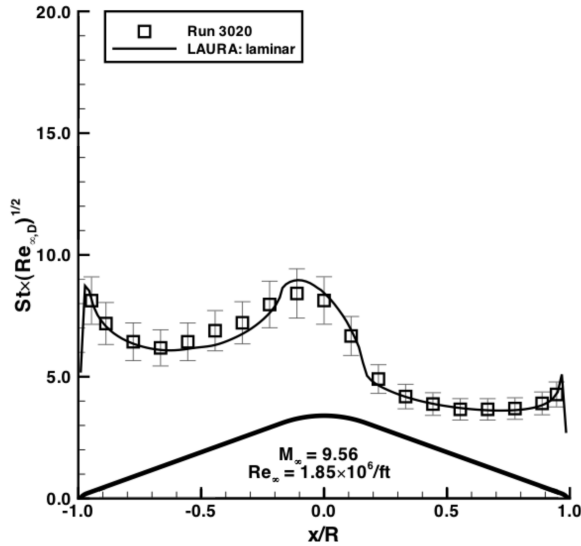


Fig. 14 Comparison for Mach 10 nozzle, $Re_{\infty} = 1.85 \times 10^6$ 1/ft, $\alpha = 16$ deg.

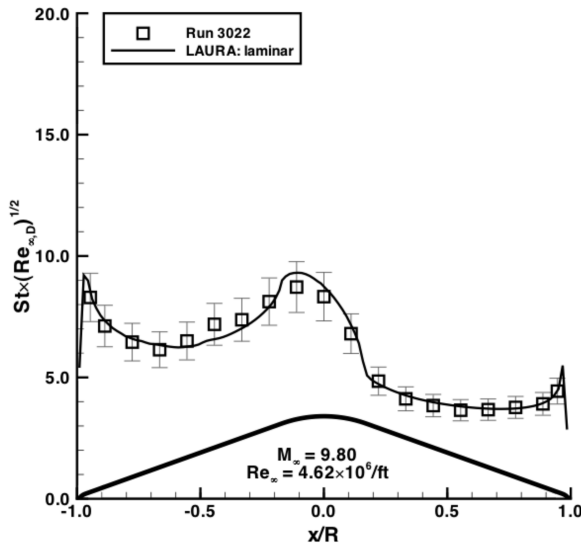


Fig. 15 Comparison for Mach 10 nozzle, $Re_{\infty} = 4.62 \times 10^6$ 1/ft, $\alpha = 16$ deg.

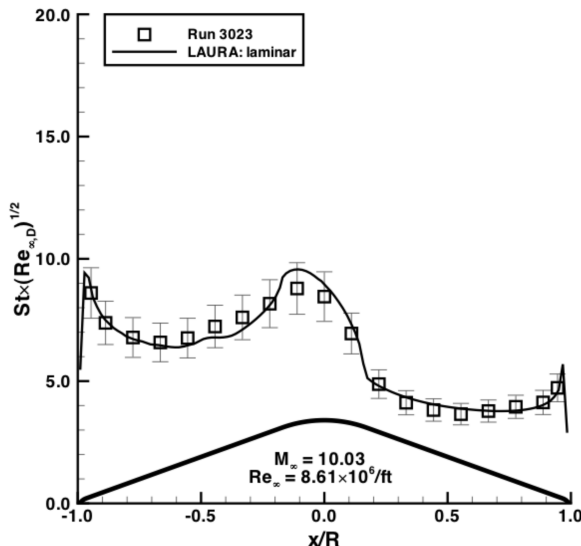


Fig. 16 Comparison for Mach 10 nozzle, $Re_{\infty} = 8.61 \times 10^6$ 1/ft, $\alpha = 16$ deg.

augmentation in the wind-side stagnation region ($x/R \sim 0.4$) such as was noted in [7].

The Mach 8 comparisons are more difficult to interpret because it is unclear whether any of the conditions provided a completely laminar case. At the four highest Reynolds number Mach 8 cases (Figs. 21–24), the data appeared to be turbulent on the lee side of the model and a good match with turbulent predictions (within the $\pm 12\%$ experimental uncertainty) was observed. Also, at the highest two Reynolds numbers, the data on the wind side appeared to be turbulent and a close match with turbulent predictions was again observed. These two cases are thought to be the only experimental data set in which fully turbulent flow over the complete forebody has been observed for a large-angle, blunted sphere-cone geometry such as MSL. The contention that these data are turbulent is supported by the very high Re_{θ}/M_e and Re_{θ} values shown in Fig. 12. In contrast to the good agreement at high Reynolds number turbulent conditions, the data and the laminar predictions for the two lowest Reynolds number (Figs. 19 and 20) conditions differed significantly. However, Re_{θ}/M_e and Re_{θ} values for these two cases are close to those for the Mach 10 cases at which transitional effects were observed, and so it is possible that these data are nonlaminar. The operating envelope of this nozzle did not permit testing at even lower Reynolds numbers to ensure the presence of completely laminar flow for the current model scale.

As with the Mach 10 comparisons, the Mach 8 comparisons also showed that measured heating values in the wind-side stagnation region exhibited a nonlaminar heating augmentation that was not predicted by the computations. As this behavior has been noted in other studies in different wind tunnels, this result suggests a deficiency in the turbulence models used for the study rather than a facility-related issue. However, this phenomena does not appear to be a mission design concern because the flight heating methodology is to perform fully turbulent computations over the whole vehicle and take the highest (lee side) turbulent levels as the design value. The stagnation region augmentation, whatever its cause, is much lower than that predicted for the turbulent lee side.

B. NASA LaRC 20 Inch Mach 6 Air Tunnel Heating Data and CFD Comparisons

Results from the LaRC 20 Inch Mach 6 Air Tunnel test are compared with laminar predictions in Figs. 25–29. Only laminar predictions are shown for these cases because the model appeared to remain laminar for all test conditions except at the highest Reynolds number of $Re_{\infty} = 6.9 \times 10^6$ ft (Fig. 29) where the flow became transitional on the lee side just before the corner. Centerline Re_{θ} and Re_{θ}/M_e values for these cases are plotted in Fig. 30. These values are in the same range as the lowest AEDC Tunnel 9 Mach 10 nozzle conditions, for which laminar flow was also observed. In general, predictions and wind-tunnel data were again within the estimated $\pm 12\%$ experimental uncertainty except around the nose and stagnation region for some of the cases. A possible reason for this poorer comparison in these areas is that the run time in the LaRC 20 Inch Mach 6 Air Tunnel was longer than that in the AEDC Tunnel 9 (~ 5 s as compared with ~ 1 s), due to the length of time required to inject the model into the test section. The wind-tunnel model wall thickness was only designed to satisfy the semi-infinite conduction assumption (i.e., the temperature rise within the model does not reach the back face) for AEDC Tunnel 9 test durations, and so the longer Mach 6 test time introduced errors into the analysis. As a result of this study, the operating sequence for thermocouple testing in this facility has been modified to permit faster model injection and thus reduce the total test length to avoid violating the semi-infinite assumption. Additionally, the procedure will call for shorter angle-of-attack sweeps which will also reduce the test length.

V. Summary and Conclusions

An experimental investigation of aerodynamic heating to the forebody of the MSL entry vehicle was conducted in the Mach 10 and Mach 8 nozzles of AEDC Tunnel 9 and laminar, transitional, and turbulent data were obtained. The purpose of this test was to determine the baseline accuracy with which the computational tools

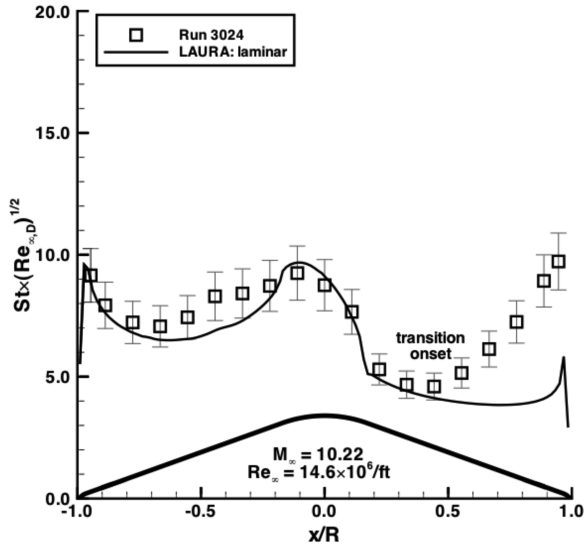


Fig. 17 Comparison for Mach 10 nozzle, $Re_{\infty} = 14.6 \times 10^6$ 1/ft, $\alpha = 16$ deg.

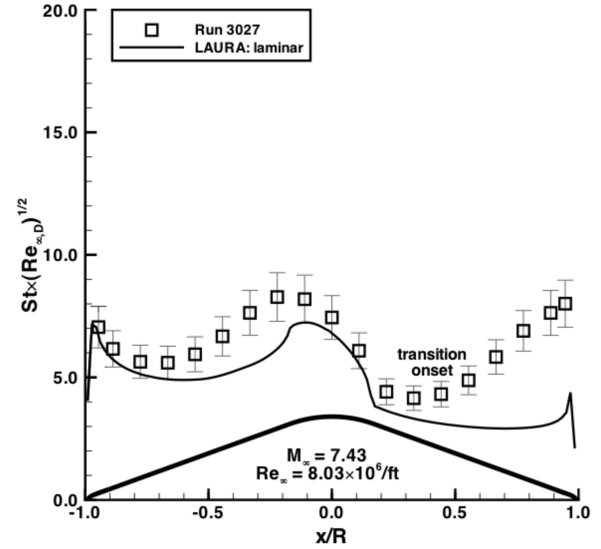


Fig. 20 Comparison for Mach 8 nozzle, $Re_{\infty} = 8.03 \times 10^6$ 1/ft, $\alpha = 16$ deg.

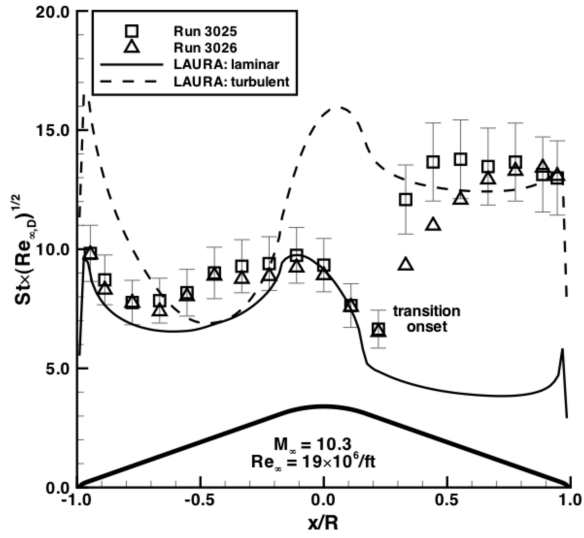


Fig. 18 Comparison for Mach 10 nozzle, $Re_{\infty} = 19 \times 10^6$ 1/ft, $\alpha = 16$ deg.

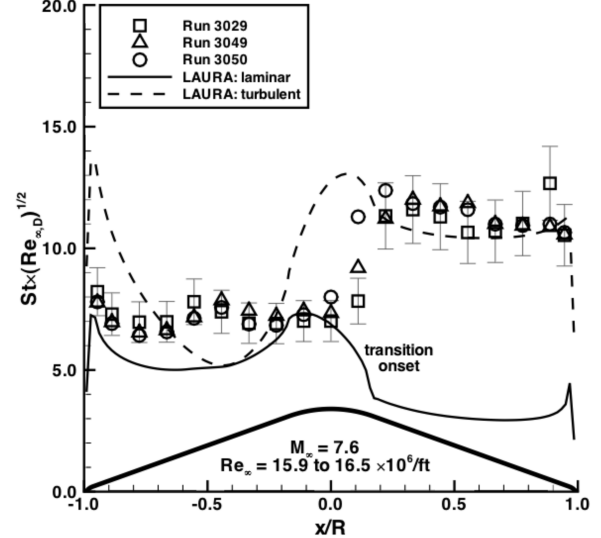


Fig. 21 Comparison for Mach 8 nozzle, $Re_{\infty} = 16 \times 10^6$ 1/ft, $\alpha = 16$ deg.

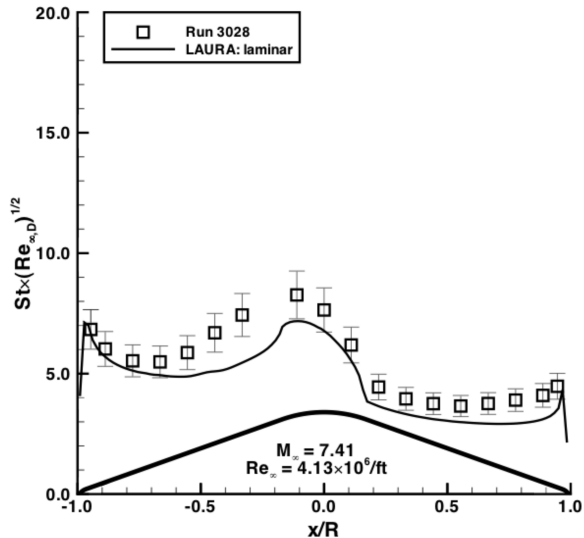


Fig. 19 Comparison for Mach 8 nozzle, $Re_{\infty} = 4.13 \times 10^6$ 1/ft, $\alpha = 16$ deg.

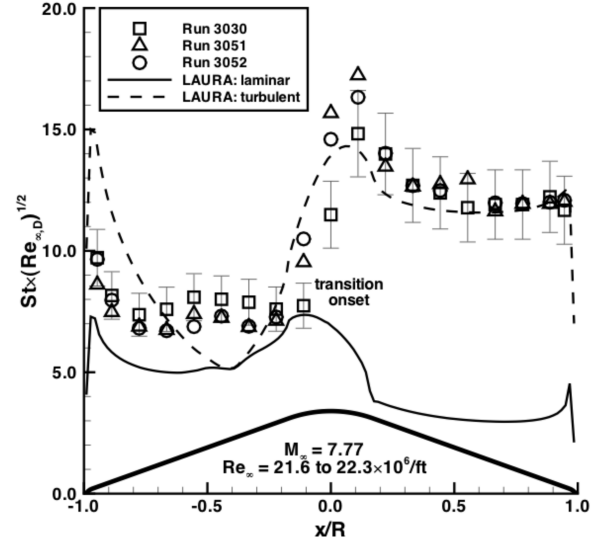


Fig. 22 Comparison for Mach 8 nozzle, $Re_{\infty} = 22 \times 10^6$ 1/ft, $\alpha = 16$ deg.

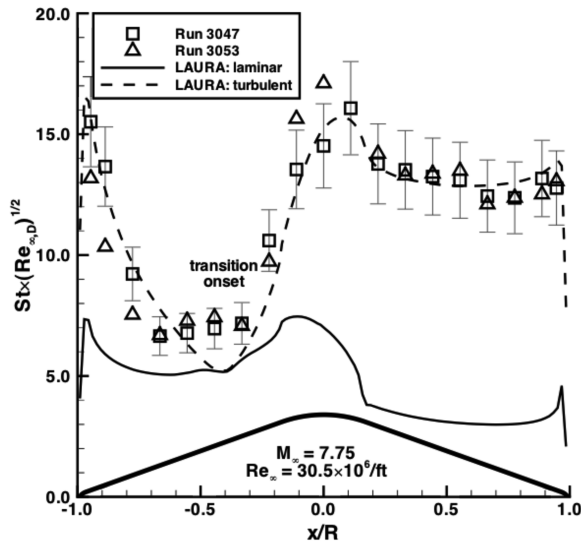


Fig. 23 Comparison for Mach 8 nozzle, $Re_{\infty} = 30.5 \times 10^6$ 1/ft, $\alpha = 16$ deg.

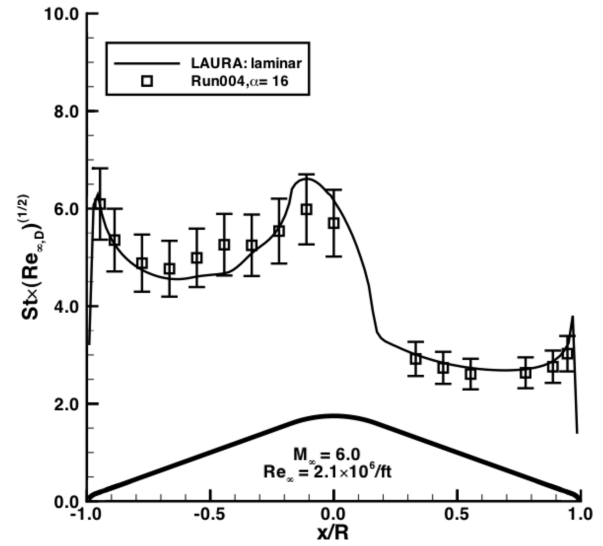


Fig. 26 Comparison for LaRC 20 Inch Mach 6 Air Tunnel, $Re_{\infty} = 2.1 \times 10^6$ 1/ft, $\alpha = 16$ deg.

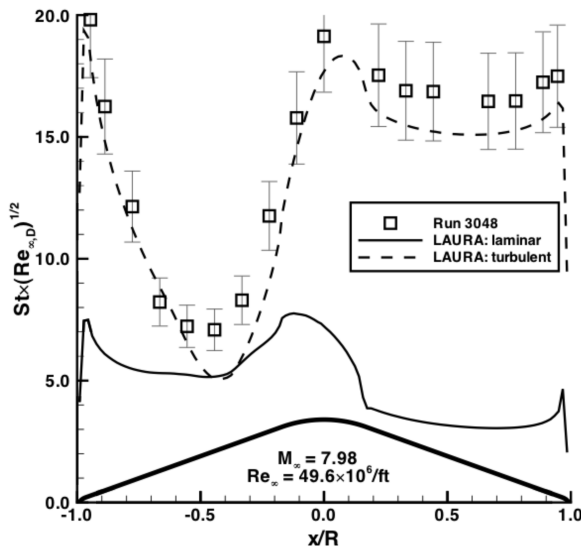


Fig. 24 Comparison for Mach 8 nozzle, $Re_{\infty} = 49.6 \times 10^6$ 1/ft, $\alpha = 16$ deg.

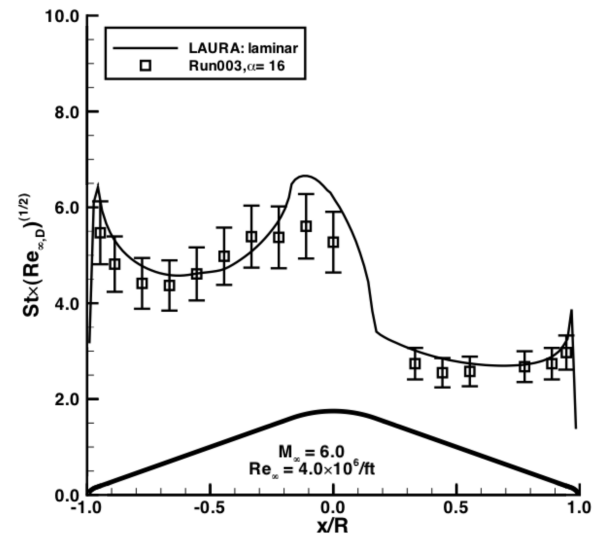


Fig. 27 Comparison for LaRC 20 Inch Mach 6 Air Tunnel, $Re_{\infty} = 4.0 \times 10^6$ 1/ft, $\alpha = 16$ deg.

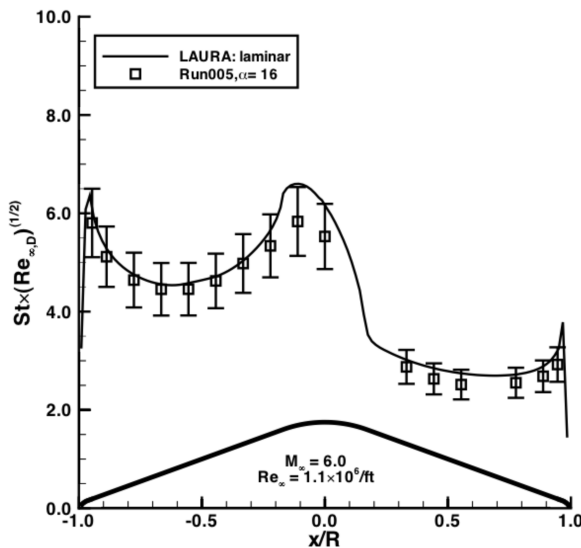


Fig. 25 Comparison for LaRC 20 Inch Mach 6 Air Tunnel, $Re_{\infty} = 1.1 \times 10^6$ 1/ft, $\alpha = 16$ deg.

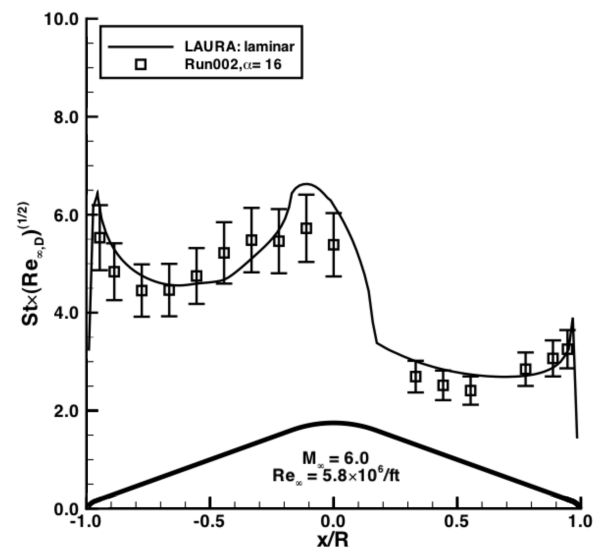


Fig. 28 Comparison for LaRC 20 Inch Mach 6 Air Tunnel, $Re_{\infty} = 5.8 \times 10^6$ 1/ft, $\alpha = 16$ deg.

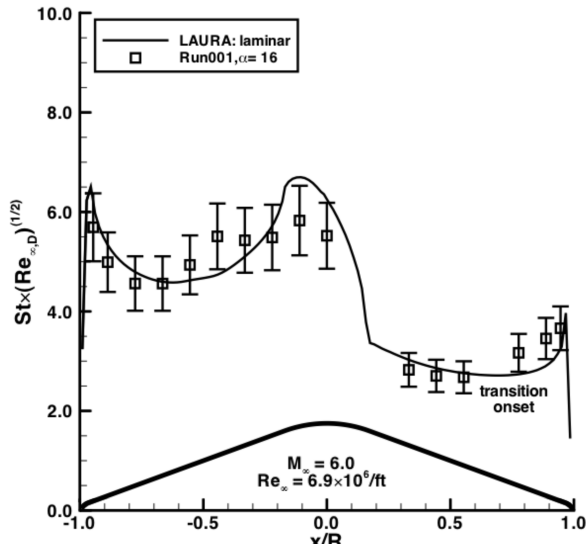


Fig. 29 Comparison for LaRC 20 Inch Mach 6 Air Tunnel, $Re_{\infty} = 6.9 \times 10^6$ 1/ft, $\alpha = 16$ deg.

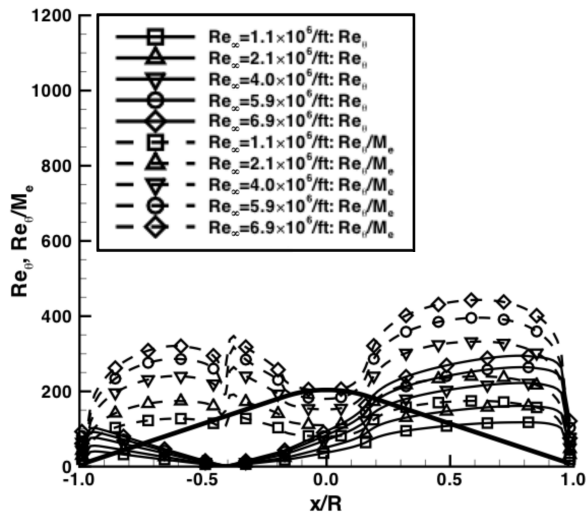


Fig. 30 Boundary-layer parameters for LaRC 20 Inch Mach 6 Air Tunnel conditions.

being used in the design of the MSL vehicle could predict turbulent heating levels in an environment free from the uncertainties produced in a high-enthalpy, nonequilibrium impulse facility.

Heating data were obtained using coaxial thermocouples, and comparisons were made with laminar and turbulent CFD predictions. The measurements and predictions were found to compare to within the estimated $\pm 12\%$ experimental uncertainty for cases when either fully laminar or fully turbulent flow was produced, except at the two lowest Reynolds numbers in the Mach 8 nozzle of Tunnel 9, where it was unclear whether the data were laminar or transitional. In some of the higher Reynolds number Mach 8 and Mach 10 data, a nonlaminar augmentation of the data was observed in the wind-side stagnation region such as was observed in other test facilities, but the augmentation was not high enough to represent a design concern. The results of these comparisons will be incorporated into the design uncertainty methodology for the MSL flight program.

These good comparisons were obtained only after the effects of the model material thermal properties were investigated and it was concluded that the original material properties data used were probably incorrect. Preliminary recommendations for a new set of thermal properties for use in thermocouple data reduction were made based on these results.

To support the AEDC Tunnel 9 test, a short test was also performed in the LaRC 20 Inch Mach 6 Air Tunnel to validate the use of these

thermal properties. Predictions for the Mach 6 conditions were also generally within the $\pm 12\%$ experimental uncertainty, although, in some regions, the agreement was not as good, probably due to violation of the semi-infinite wall assumption over the longer run times required in this facility to complete a pitch sweep. As a result, the run times for future thermocouple testing in constant pitch-sweep mode will be shortened by limiting the range of the pitch sweep.

References

- [1] Lockwood, M. K., "Introduction: Mars Science Laboratory: The Next Generation of Mars Landers," *Journal of Spacecraft and Rockets*, Vol. 43, No. 2, March–April 2006, p. 257.
- [2] Lockwood, M. K., Powell, R. W., Sutton, K., Prabhu, R. K., Graves, C. A., Epp, C. D., and Carman, G. L., "Entry Vehicle Configurations and Performance for the Mars Smart Lander," *Journal of Spacecraft and Rockets*, Vol. 43, No. 2, March–April 2006, pp. 258–269.
- [3] Edquist, K. T., "Aerothermodynamic Environments Definition for the Mars Science Laboratory Entry Capsule," *45th AIAA Aerospace Sciences Meeting and Exhibit*, AIAA Paper 2007-1206, 2007.
- [4] Hollis, B. R., and Liechty, D. S., "Transition Due to Heat-Shield Cavities on a Mars Entry Vehicle," *Journal of Spacecraft and Rockets*, Vol. 43, No. 2, March–April 2006, pp. 354–366.
- [5] Liechty, D. S., Hollis, B. R., and Edquist, K. T., "Mars Science Laboratory Experimental Aerothermodynamics with Effects of Cavities and Control Surfaces," *Journal of Spacecraft and Rockets*, Vol. 43, No. 2, March–April 2006, pp. 340–353.
- [6] Wright, M. J., Olejniczak, J., Brown, J. L., Hornung, H. G., and Edquist, K. T., "Modeling of Shock Tunnel Aeroheating Data on the Mars Science Laboratory Aeroshell," *Journal of Thermophysics and Heat Transfer*, Vol. 20, No. 4, Oct.–Dec. 2006, pp. 641–646. doi:10.2514/1.19896
- [7] Hollis, B. R., Liechty, D. S., Wright, M. J., Holden, M. S., Wadhams, T. P., MacLean, M., and Dyakonov, A., "Transition Onset and Turbulent Aeroheating Measurements on the Mars Science Laboratory Entry Vehicle," AIAA Paper 2005-1437, Jan. 2005.
- [8] Marren, D., and Lafferty, J., "AEDC Hypervelocity Wind Tunnel 9," *Advanced Hypersonic Test Facilities*, Vol. 198, Progress in Aeronautics and Astronautics, AIAA, Reston, VA, 2002, pp. 467–477.
- [9] Micol, J. R., "Langley Aerothermodynamic Facilities Complex: Enhancements and Testing Capabilities," AIAA Paper 98-0147, Jan. 1998.
- [10] Hedlund, E. R., Hill, J. A. F., Ragsdale, W. C., and Voisin, R. L. P., "Heat Transfer Testing in the NSWC Hypervelocity Wind Tunnel Utilizing Co-Axial Surface Thermocouples," Naval Surface Weapons Center NSWC-MP-80-151, March 1980.
- [11] Boyd, C. F., and Howell, A., "Numerical Investigation of One-Dimensional Heat-Flux Calculations," Naval Surface Warfare Center NSWCDD/TR-94/114, Oct. 1994.
- [12] Hollis, B. R., "User's Manual for the One-Dimensional Hypersonic Aero-Thermodynamic (1DHEAT) Data Reduction Code," NASA CR-4691, Aug. 1995.
- [13] Coblish, J. C., "Aerothermal Measurement Improvements Using Coaxial Thermocouples at AEDC Hypervelocity Wind Tunnel No. 9," *45th AIAA Aerospace Sciences Meeting and Exhibit*, AIAA Paper 2007-1467, Jan. 2007.
- [14] Gnoffo, P. A., "Upwind-Biased, Point-Implicit Algorithm for Viscous, Compressible Perfect-Gas Flows," NASA TP-2953, Feb. 1990.
- [15] Cheatwood, F. M., and Gnoffo, P. A., "User's Manual for the Langley Aerothermodynamic Upwind Relaxation Algorithm (LAURA)," NASA TM 4674, April 1996.
- [16] Roe, P. L., "Approximate Riemann Solvers, Parameter Vectors and Difference Schemes," *Journal of Computational Physics*, Vol. 43, No. 2, 1981, pp. 357–372. doi:10.1016/0021-9991(81)90128-5
- [17] Harten, A., "High Resolution Schemes for Hyperbolic Conservation Laws," *Journal of Computational Physics*, Vol. 49, No. 3, 1983, pp. 357–393. doi:10.1016/0021-9991(83)90136-5
- [18] Yee, H. C., "On Symmetric and Upwind TVD Schemes," NASA TM 88325, 1990.
- [19] Brown, J. L., "Turbulence Model Validation for Hypersonic Flows," *8th AIAA/ASME Joint Thermophysics and Heat Transfer Conference*, AIAA Paper 2002-3308, June 2002.